Applied Catalysis B: Environmental 331 (2023) 122655

Contents lists available at ScienceDirect

Applied Catalysis B: Environmental

journal homepage: www.elsevier.com/locate/apcatb

# Sustainable self-powered degradation of antibiotics using $Fe_3O_4$@$MoS_2$/PVDF modified pipe with superior piezoelectric activity: Mechanism insight, toxicity assessment and energy consumption

Jingxue Wang [a], Xiaonan Zhou [a], Juncheng Hao [a], Zichen Wang [a], Bingjie Huo [a], Jianguang Qi [a], Yinglong Wang [a,*], Fanqing Meng [a,*]

[a] College of Chemical Engineering, Qingdao University of Science and Technology, Qingdao 266042, China

ARTICLE INFO

*Keywords:*
Piezocatalytic pipe
Water flow energy
Self-powered
Piezocatalytic degradation
Wastewater treatment

ABSTRACT

Using clean energy from the environment to treat organics is a sustainable approach to alleviate the energy shortage and environmental pollution. Water flow energy in pipelines is overlooked due to the lack of efficient energy-converting material. Herein, a novel $Fe_3O_4$ @$MoS_2$/PVDF modified pipe was prepared and used for self-powered piezocatalytic degradation of organics in the pipeline. The degradation efficiency of tetracycline, Rhodamine B, ciprofloxacin and oxytetracycline can reach 92.5 %, 90.9 %, 85.9 % and 69.2 %, respectively, at an ultralow flow rate. The energy consumption of this water treatment system was only 12.7 % of that of ultrasonic systems. The theoretical calculation and characterization results indicated that the ultrahigh piezocatalytic efficiency was derived from the coupling effect of $Fe_3O_4$/$MoS_2$ and PVDF. EPR results showed that $\bullet O_2^-$, $\bullet OH$, and $h^+$ were the main active species in degrading organics. The results of the toxicity assessment showed that ecotoxicity could be reduced or even eliminated.

## 1. Introduction

As one of the most common organic pollutants in water, a variety of antibiotics have been detected in wastewater [1], river water [2], surface water [3], and seawater [4] in recent years. The persistence of antibiotics in the aquatic environment will lead to the risk of antibiotic resistance, which will pose a potential threat to the ecological environment and human health, so the removal of antibiotics is becoming increasingly urgent [5].

Piezocatalysis has gradually developed into an effective organic wastewater treatment technology with its characteristics of low energy consumption and low pollution [6–10]. $MoS_2$ has excellent piezoelectric response because of its layered structure with single or few layers and central asymmetric lattice [11,12], and has been extensively used to degrade organic pollutants in wastewater [13–15]. $Fe_3O_4$ is a traditional transition metal oxide nanoparticle with a matching band structure that can enhance the separation of photogenerated charge and increase the quantum transport rate [16]. Polyvinylidene fluoride (PVDF), as one of the most widely studied piezoelectric polymers, has gradually attracted the interest of researchers in the field of organic pollutant degradation [17]. Wan et al. [18] prepared a piezoelectric polymer film with $BaTiO_3$ nanocubes embedded in PVDF, which showed an efficient piezocatalytic degradation of bisphenol A under ultrasonic vibration. Singh et al. [19] successfully prepared Ag@$LiNbO_3$/PVDF composite membranes, which demonstrated the potential of piezoelectric catalytic degradation of tetracycline and ciprofloxacin under ultrasonic conditions.

At present, the ultrasonic process is a traditional water treatment method with high degradation efficiency [20–22]. However, the ultrasonic piezocatalytic process is not suitable for large-scale wastewater treatment because of its unique noise and relatively high energy consumption. Tang et al. [23] used a ball mill as an external force source to achieve 90.0 % effective degradation of ciprofloxacin and norfloxacin for layered $Pb_2BO_3I$ piezoelectric materials within 15 min, demonstrating that the powerful force generated by the collision of mill balls played an important role in the charge separation process. Li et al. [24] successfully prepared CuS/$MoS_2$ nanocomposites with excellent piezoelectric properties, which could completely remove Cr (VI) and RhB within 180 s under mechanical agitation in the dark. Although ball milling and agitation as external forces have been proven to be effective methods of piezocatalytic degradation of organic pollutants, it is worth

* Corresponding authors.
*E-mail addresses:* wangyinglong@qust.edu.cn (Y. Wang), 03589@qust.edu.cn (F. Meng).

https://doi.org/10.1016/j.apcatb.2023.122655
Received 12 January 2023; Received in revised form 12 March 2023; Accepted 15 March 2023
Available online 5 April 2023

noting that the strong shear force of ball milling may damage the structure of the catalyst and lead to its unsatisfactory reusability. In addition, the degradation efficiency of pollutants by the agitation method needs to be improved. Besides, the lack of efficient energy collection and conversion materials leads to the neglect of water flow energy in pipeline systems and the natural environment. So, it is imperative to find a water treatment method with a high energy utilization rate, green, and low cost.

In this work, a novel $Fe_3O_4$@$MoS_2$/PVDF modified pipe powered by water flow with excellent piezocatalytic performance was prepared. The self-powered piezoelectric pipe system collected energy from water flow and converted mechanical energy into electrical energy for efficient degradation of organics. The finite element method was used to explore the reasons for the enhancement of the piezocatalytic activity of the pipe. The removal rates of tetracycline, rhodamine B, ciprofloxacin, and oxytetracycline reached 92.5 %, 90.9 %, 85.9 %, and 69.2 %, respectively. Meanwhile, the influence of pH, water velocity, coexisting anions and water matrixes on the degradation were investigated. The energy consumption EE/O of the piezocatalytic process was compared, which showed that the energy consumption of this system was the lowest. Electron paramagnetic resonance was analyzed with the active radicals produced during the process of piezocatalysis and the possible degradation mechanism was further proposed. The main content of this study is shown in Fig. 1.

## 2. Experimental section

### 2.1. Synthesis of $Fe_3O_4$@$MoS_2$

$Fe_3O_4$@$MoS_2$ was synthesized by a two-step method. Step 1: $Fe_3O_4$ powder was synthesized according to the reported method [25]. Step 2: 0.690 g $CH_4N_2S$ and 0.615 g $Na_2MoO_4$ were firstly dissolved in 30 mL deionized water and then adjusted pH to 3.5 with 0.5 mol/L HCl and stirred continuously for 30 min to get solution A. 0.1 g completely dried $Fe_3O_4$ powder was placed in solution A. Ultrasonic treatment was conducted for 10 min to make it evenly dispersed, and suspension B was obtained. Finally, the suspension B was transferred to a 100 mL Teflon reactor and reacted at 200 ℃ for 24 h. After the reaction, the product was centrifuged repeatedly, washed with water and ethanol 3 times, and finally dried at 60 ℃ for 12 h.

### 2.2. Synthesis of $Fe_3O_4$@$MoS_2$/PVDF piezoelectric pipe

As shown in Figs. S1, 2g PVDF powders were placed in 20 mL N, N-dimethylformamide (DMF), heated, and stirred to completely dissolve. Then 0.2 g $Fe_3O_4$ @$MoS_2$ powders were added to the above solution and stirred for 2 h. After the suspension was evenly mixed, it was uniformly rotated into a 2 m Teflon pipe with uniform rotation and deionized water was poured into the pipe in the same way. At last, $Fe_3O_4$@$MoS_2$/PVDF was uniformly combined on the wall of the pipe by phase transformation method.

### 2.3. Characterization

The morphology of catalyst samples prepared was observed using scanning electron microscopy (SEM, Japan) and the crystal structure was analyzed by D/MAX/2500PC X-ray diffraction (XRD, Japan) and Fourier transform infrared spectroscopy (FTIR). X-ray photoelectron spectroscopy (XPS, ESCALAB 250, Fisher Scientific, USA) was used to analyze the elemental composition, content, atomic valence state, and other information of the compounds. Piezoelectric coefficient $d_{33}$ was used to measure by a quasi-static $d_{33}$ measuring instrument (YE2730A, China). Piezoelectric response performance was measured by PFM (BioScope, Bruker, Ltd.). Active radicals were detected using an electron paramagnetic resonance instrument (EPR, Bruker A200, America). The intermediates were identified by liquid chromatography-tandem mass spectrometry (LC-MS, LCMS-2010A, Japan) to infer the possible degradation pathways of organic pollutants. An inductively coupled plasma mass spectrometer (ICP-MS, Agilent 7850) was used to test possible metal ion release in TC solution.

### 2.4. Piezocatalytic activities of self-powered $Fe_3O_4$@$MoS_2$/PVDF piezoelectric pipe

Herein, 20 mg/L TC, RhB, CIP, and OTC stock solutions were prepared and stored under dark conditions to evaluate the piezocatalytic activity of the $Fe_3O_4$@$MoS_2$/PVDF piezoelectric pipe. The degradation experiment was conducted by using a peristaltic pump to circulate water in the piezoelectric pipe. The actual photo of the experimental device was illustrated in Fig. 2a. 200 mL TC, RhB, CIP, and OTC solutions were taken and continuously flowed respectively in the pipe. Each cycle flow experiment lasted for 100 min. The effect of different water matrixes on degradation was studied. In addition, the effects of water velocity, initial pH of organics solution, and coexisting anions on degradation

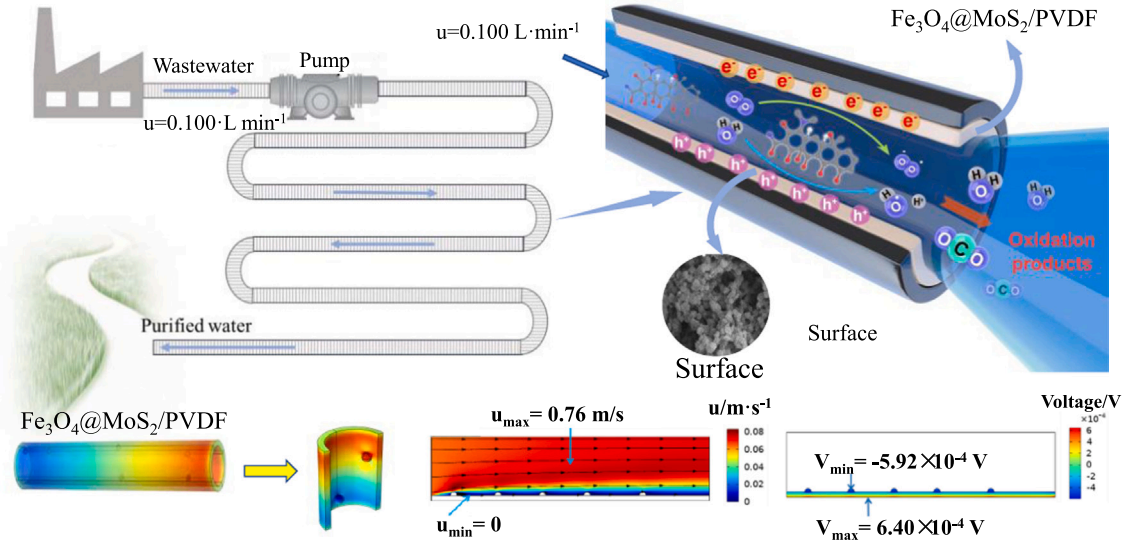


**Fig. 1.** Schematic diagram of the main content of this study.

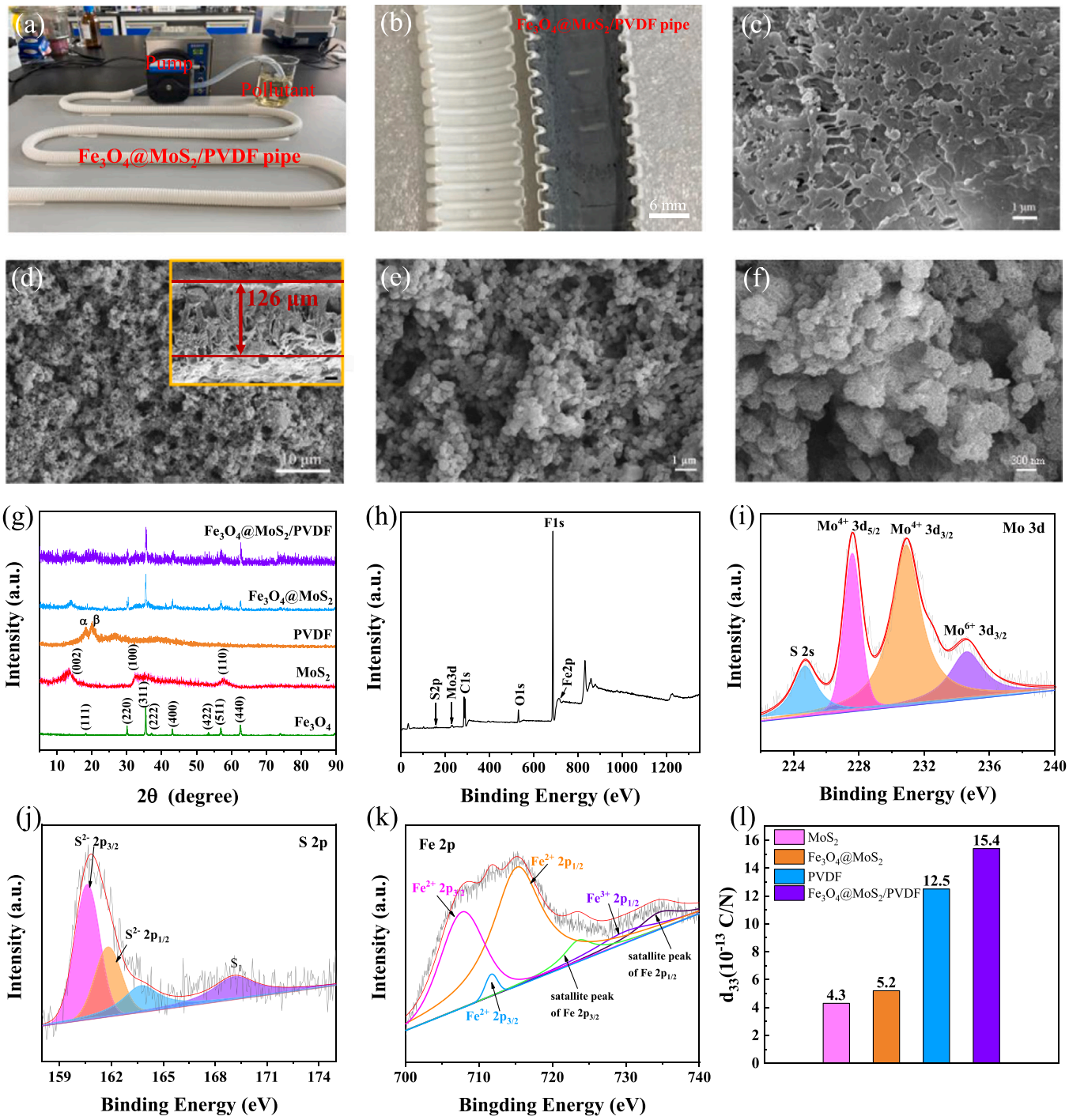


**Fig. 2.** Actual photo of (a) experimental device and (b) $Fe_3O_4$@$MoS_2$/PVDF pipe. SEM images of (c) PVDF and (d), (e), (f) $Fe_3O_4$@$MoS_2$/PVDF. (g) XRD patterns of catalyst samples. (h) XPS spectra of $Fe_3O_4$@$MoS_2$/PVDF, (i) Mo 3d, (j) S 2p and (k) Fe 2p. (l) $d_{33}$ of catalyst samples.

performance were further investigated. 3 mL of the reaction solution was collected every 10 min and filtered by a needle filter with an aperture of 0.45 μm. The concentration of organics was determined by high performance liquid chromatography (Agilent 1220LC G4290C). The mobile phase was composed of 30 % methanol and 70 % 0.01 mol/L oxalic acid solution at a flow rate of 1 mL $min^{-1}$, and the column temperature was kept at 30 ℃. The column was 150 × 4.6 mm filled with C18 silicon-based stationary phase with a particle size of 2 μm. The injection volume of all standards and samples was 5 μL. The piezocatalytic activity of $Fe_3O_4$ @$MoS_2$/PVDF was evaluated using Eq.1, The kinetic rate constants of all TC degradation experiments were calculated by Eq. S1 and Eq. S2.

$$\eta = (1 - C_t/C_0) \times 100\% \quad (1)$$

where $C_0$ (mg/L) represents the initial concentration of TC and $C_t$ (mg/L) is the concentration at the time t.

### 2.5. Theory calculations

DFT calculation in this work was based on B3LYP functional, 6–31 G basis set, and Multiwfn [26,27], DFT-D3 correction was performed. Finite element method simulation of piezoelectric properties was used to

simulate the voltage potential of materials triggered by water flow.

## 3. Results and discussion

### 3.1. Characterization

The SEM image of $MoS_2$ was shown in Fig. S2a, which showed a nanoflower-like structure. Fig. S2b was the SEM image of $Fe_3O_4$@$MoS_2$. The lamellar structure of $MoS_2$ was clearer and more active surfaces were exposed after $Fe_3O_4$ was combined with $MoS_2$ nanoflower, which was beneficial to the catalytic reaction. The actual photo of the $Fe_3O_4$@$MoS_2$/PVDF pipe (Fig. 2b) indicated that the black $Fe_3O_4$@-$MoS_2$/PVDF fitted tightly to the inner wall of the pipe. Fig. 2c showed the SEM image of pure PVDF, whose surface was rough and compact, and the pore structure was not obvious. The images of $Fe_3O_4$@$MoS_2$/PVDF were shown in Fig. 2d-f. The cross-section image (Fig. 2d) showed abundant pore structures with a film thickness of 126 μm. PVDF successfully combined with $Fe_3O_4$@$MoS_2$, as shown in Fig. 2e and f, which provided a large substrate for $Fe_3O_4$@$MoS_2$.

The XRD patterns of $Fe_3O_4$, $MoS_2$, $Fe_3O_4$@$MoS_2$, PVDF and $Fe_3O_4$@$MoS_2$/PVDF were presented in Fig. 2g. The peaks of $Fe_3O_4$ were located at 18.3° (111), 30.1° (220), 35.4° (311), 37.0° (222), 43.0° (400), 53.4° (422), 56.9° (511) and 62.5° (440), which was consistent with the $Fe_3O_4$ standard card (PDF#89–0688). The peaks at 16.6°, 32.65°, and 57.33°, corresponding to the (002), (100) and (001) planes of $MoS_2$, respectively [28]. There were two strong peaks at 18.5° and 20.7°, corresponding to the α phase and β phase of PVDF, respectively [29]. It can be observed that $Fe_3O_4$@$MoS_2$ retained the characteristic peaks of $Fe_3O_4$ and $MoS_2$, indicating that $Fe_3O_4$@$MoS_2$ reserved the crystal shape and phase of $Fe_3O_4$ and $MoS_2$ successfully. However, the peak of $Fe_3O_4$@$MoS_2$/PVDF was messy and not obvious, which may be related to the low catalyst loading during the preparation process. The FTIR spectra was shown in Fig. S3. The absorption bands of PVDF powder appeared at 763 $cm^{-1}$ and 976 $cm^{-1}$, corresponding to typical non-polar $\alpha$-phase vibration characteristics. The absorption bands at 840 $cm^{-1}$ and 1276 $cm^{-1}$ correspond to polar $\beta$-phases, confirming the coexistence of $\alpha$ and $\beta$-phases in PVDF powder. Fig. S3 clearly showed that the $\beta$-phase intensity of $Fe_3O_4$ @$MoS_2$/PVDF increases significantly, indicating that the simple phase transformation method can induce the transformation of $\alpha$- to $\beta$-phase, which also strongly proved that the incorporation of $Fe_3O_4$@$MoS_2$ can significantly increase the content of PVDF piezoelectric $\beta$-phase [22].

Fig. 2h showed the XPS survey scan of $Fe_3O_4$@$MoS_2$/PVDF, it can be seen that no other impurities exist in the prepared piezoelectric catalyst. Due to the high intensity of the F peak, S and Mo peaks were low, which may be due to the low loading of $Fe_3O_4$@$MoS_2$ in the PVDF preparation process. Peak fitting of Mo, S, and Fe was performed. Fig. 2i showed the Mo 3d spectra and peaks at 227.6 and 130.9 eV were $Mo^{4+}$ $3d_{5/2}$ and $Mo^{4+}$ $3d_{3/2}$ of $MoS_2$, respectively [30,31]. The peak at 224.7 eV was the S 2 s of $MoS_2$. The peak at 234.46 eV was $Mo^{6+}$ $3d_{3/2}$, which may be caused by partial oxidation of $MoS_2$ [31]. Fig. 2j showed the S 2p spectra. The peaks located at 160.6 and 161.8 eV were $S^{2-}$ $2p_{3/2}$ and $S^{2-}$ $2p_{1/2}$ of $MoS_2$, respectively. The peak near 168.9 eV indicated that part of the S element on the surface of $MoS_2$ was oxidized [32]. The peak near 163.7 eV was the unsaturated S element on the $MoS_2$ surface. Fig. 2k showed the Fe 2p spectra. Peaks located at 707.3, 712.2, 715.5 and 728.2 eV were $Fe^{2+}$ $2p_{3/2}$, $Fe^{3+}$ $2p_{3/2}$, $Fe^{2+}$ $2p_{1/2}$ and $Fe^{3+}$ $2p_{1/2}$, respectively. Peaks at 722.4 and 733.5 eV were the satellite peaks of Fe $2p_{3/2}$ and Fe $2p_{1/2}$, respectively [33].

### 3.2. Piezoelectric properties

The piezoelectric coefficient $d_{33}$ [34] of catalyst samples was studied in order to intuitively evaluate their piezoelectric properties. The $d_{33}$ of $MoS_2$ reached $4.3 \times 10^{-13}$ C/N, while the $d_{33}$ of $Fe_3O_4$@$MoS_2$ was 17.3 % higher than that of $MoS_2$, as shown in Fig. 2l. The presence of $Fe_3O_4$@$MoS_2$ increased the $d_{33}$ of PVDF by 18.8 % compared with that of PVDF, which could be attributed to the increase of $\beta$-phase content in PVDF. The high $d_{33}$ of $Fe_3O_4$@$MoS_2$/PVDF indicated its excellent piezoelectric properties. Fig. 3a-b demonstrated the height signal of the topography images and piezoelectric response of $Fe_3O_4$@$MoS_2$/PVDF, respectively. These results confirm that $Fe_3O_4$@$MoS_2$/PVDF has better piezoelectric properties than $Fe_3O_4$@$MoS_2$ (Fig. S4a-b). In addition, Fig. S4c showed that the piezoelectric response amplitude of $Fe_3O_4$@-$MoS_2$/PVDF was high. These results are consistent with the $d_{33}$ measurement results. In conclusion, $Fe_3O_4$ @$MoS_2$/PVDF pipe had a high piezoelectric performance, which indirectly proves the increase of $\beta$-phase content in PVDF.

### 3.3. Piezoelectric performance simulation

Piezoelectric potential is the dominant factor in degrading organic pollutants. In general, the higher the piezoelectric potential, the stronger the decomposition ability of organic pollutants [35]. Qualitative analysis of the piezoelectric potential of piezoelectric pipe material and the velocity distribution, pressure distribution, and the generated electric potential distribution of pollutant solutions flowing through the pipe based on finite element simulation. Detailed parameter settings for the simulation are provided in Text S2. As shown in Fig. 3c-d, compared with pure PVDF pipe (8 V), the surface potential difference of $Fe_3O_4$@$MoS_2$/PVDF pipe was improved by 33.3 % (12 V). It can be seen from Figs. 3e and h, that compared with the maximum velocity of the PVDF pipe (0.096 m/s), the velocity of the $Fe_3O_4$@$MoS_2$/PVDF system decreased to 0.076 m/s. However, as shown in Figs. 3f and i, the $Fe_3O_4$@$MoS_2$/PVDF pipe generated a higher fluid pressure, which was beneficial for increasing the degree of deformation of the piezoelectric catalyst and thus improving its piezoelectric response. At the microscopic level, as shown in the SEM images of the catalysts in Fig. 2, the surface of $Fe_3O_4$@$MoS_2$/PVDF became coarser, which can increase the disturbance of water flow to a certain extent and promote the probability of contact between active radicals and pollutant molecules. As shown in Fig. 3g and j, compared with the PVDF pipe ($1.22 \times 10^{-3}$ V), the potential difference generated by $Fe_3O_4$@$MoS_2$/PVDF pipe was increased to $1.23 \times 10^{-3}$ V. The larger surface potential indicated that $Fe_3O_4$@$MoS_2$/PVDF pipe may be more conducive to the separation of electron-holes on the catalyst surface to degrade pollutants. The simulation results were basically consistent with the trend of $d_{33}$ test. In summary, from the simulation of velocity, pressure and potential distribution, it is theoretically verified that $Fe_3O_4$@$MoS_2$/PVDF pipe has high piezoelectric performance.

### 3.4. Piezocatalytic activity and effect of parameters, initial pH, and inorganic anions

To evaluate their degradation performance, pure PVDF pipe, $MoS_2$/PVDF pipe, $Fe_3O_4$/PVDF pipe, $Fe_3O_4$@$MoS_2$/PVDF pipe and $Fe_3O_4$@-$MoS_2$/PVDF pipe were prepared by the same preparation method, and degraded 20 mg/L TC respectively under the same conditions. The results were shown in Fig. 4a, the degradation of TC by pure PVDF pipe and $Fe_3O_4$/PVDF pipe was not ideal, the removal rates were 62.2 % and 75.1 %, respectively, and the reaction rates were also slow, and the apparent second-order rate constants $k$ only reached 0.365 $mM^{-1}$ $min^{-1}$ and 0.643 $mM^{-1}$ $min^{-1}$. However, $MoS_2$/PVDF pipe can achieve the removal of 80.2 % TC, and the apparent second order rate constant of the reaction was 3 times that of pure PVDF pipe. It can be clearly seen that the degradation efficiency and kinetics of $Fe_3O_4$@$MoS_2$/PVDF were significantly improved and the TC removal rate reached 92.5 %, the $k$ was 5, 2.8, and 1.6 times higher than those of pure PVDF, $Fe_3O_4$/PVDF, and $MoS_2$/PVDF pipe, respectively. The liquid chromatograms and UV–vis spectrograms of TC degradation by $Fe_3O_4$@$MoS_2$/PVDF pipe at different times were presented in Fig. S5. Considering the reaction efficiency, $Fe_3O_4$@$MoS_2$/PVDF pipe was selected for further research in

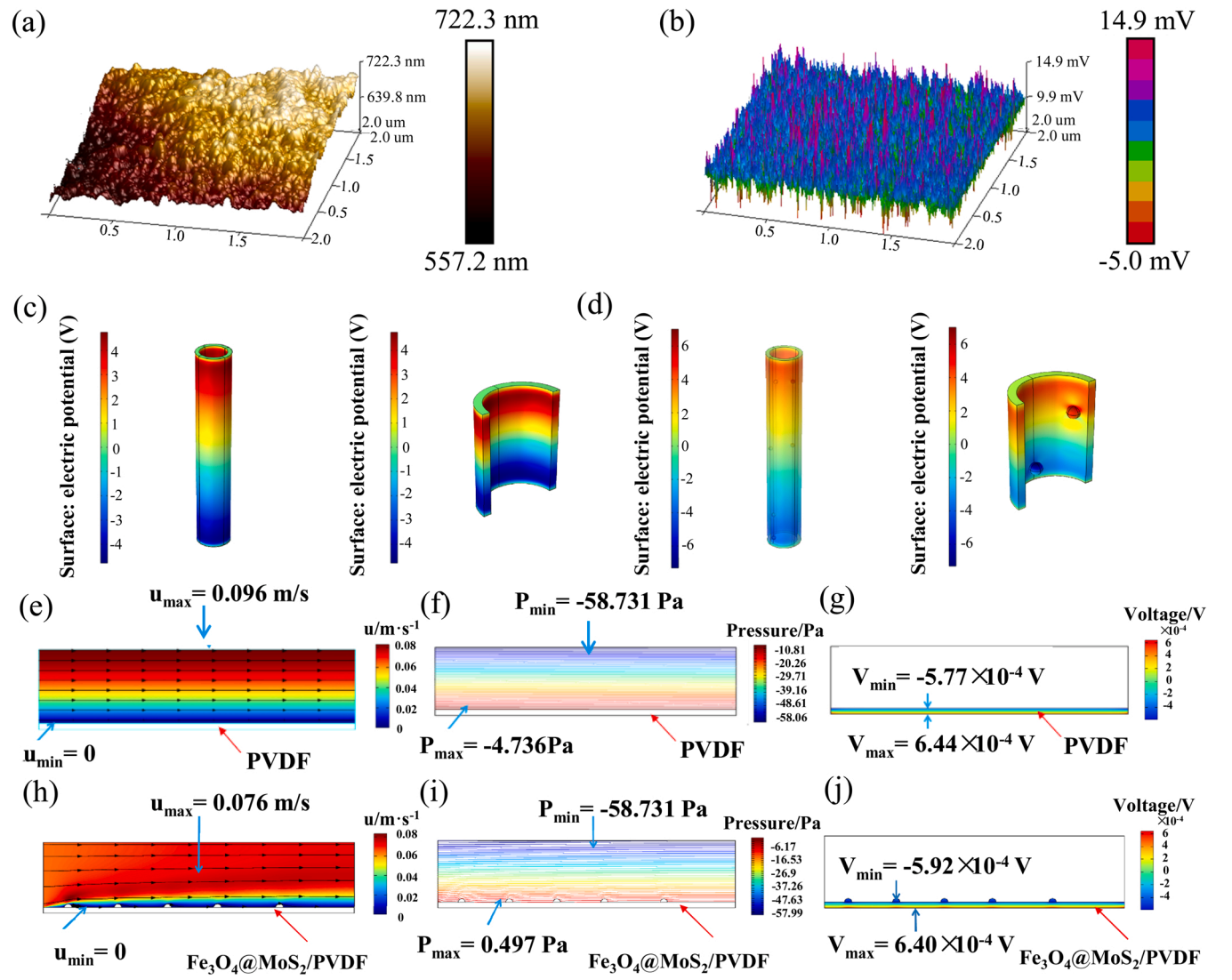


**Fig. 3.** (a) AFM images and (b) piezoelectric responsive images of $Fe_3O_4$@$MoS_2$/PVDF. Surface potential simulation of (c) PVDF pipe and (d) $Fe_3O_4$@$MoS_2$/PVDF pipe. (e)-(j) The velocity, pressure and electric potential distribution simulation results.

this experiment.

To explore the extensive degradation capability of the $Fe_3O_4$@$MoS_2$/PVDF piezoelectric pipe for different pollutants, the antibiotics tetracycline (TC), ciprofloxacin (CIP), oxytetracycline (OTC) and the dye Rhodamine B (RhB) were selected for testing. As can be observed from Fig. 4b, the OTC degradation efficiency was not ideal, with a removal rate of only 69.2 % and a $k$ of 0.612 $mM^{-1}$ $min^{-1}$. The degradation rate of CIP was 85.9 %, and the $k$ was up to 1.291 $mM^{-1}$ $min^{-1}$. Obviously, $Fe_3O_4$@$MoS_2$/PVDF piezoelectric pipe had good degradation of RhB with the fastest reaction rate due to its excellent piezocatalytic performance for dye. Video S1 showed the experimental apparatus and process demonstration of RhB degradation. The removal rate of TC reached 92.5 %, which was the highest among them. In general, $Fe_3O_4$@$MoS_2$/PVDF piezoelectric pipe had a wide range of abilities to remove organic pollutants, among which, TC had the highest degradation performance. Therefore, in this work, TC was selected as the object for subsequent research.

The effect of water matrixes on the removal rate of organic pollutants was studied. As shown in Fig. 4c, compared with deionized water, both surface water and tap water showed different degrees of inhibition on the piezocatalytic degradation of TC. In the surface water system, the degradation efficiency of TC was 89.6 %, indicating that surface water had a weak inhibitory effect. the degradation activity was reduced by 12.8 % due to chlorination byproducts in tap water, which combined with $h^+$ and •OH [36], so the oxidation of TC was inhibited. In conclusion, the water matrixes had little influence on the degradation performance of $Fe_3O_4$@$MoS_2$/PVDF piezoelectric pipe, which provided the possibility for the treatment of actual water environment.

The effects of different factors on TC degradation were discussed. The speed of the pump head was adjusted to change the flow rate. In this experiment, the flow rate was selected as 0.021, 0.062, 0.100, 0.120, 0.926, 1.299, 1.677 and 2.222 L•$min^{-1}$. As shown in Fig. 5a, the removal rates under different flow rates were 57.2 %, 73.9 %, 92.5 %, 92.3 %, 89.4 %, 99.5 %, 98.5 % and 99.5 %, respectively. When the rotational speed of the peristaltic pump was changed, its peristaltic frequency was also changed, which led to the change in fluid pulse. The experimental results of flow velocity influence showed that the degradation rate also increased with the increase of flow velocity. It can be explained that the increase of flow velocity can increase the force of the fluid on the piezoelectric catalyst, which was more beneficial to cause the polarization deformation of the piezoelectric catalyst, generating an internal electric field, promoting the separation of electrons and holes, then generated more active radicals by the redox reaction [37], the chance of collision and reaction with pollutants were significantly increased, which was more conducive to TC degradation. When changing water flow rate to 1.299 L $min^{-1}$ and greater, TC could be

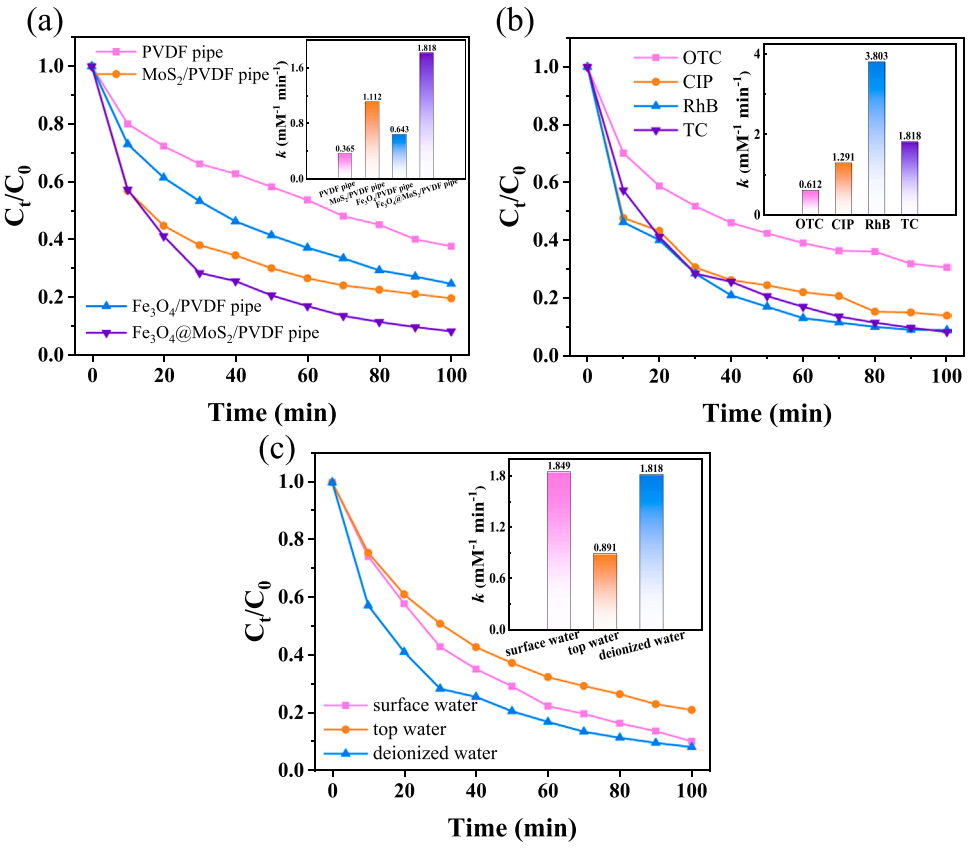


**Fig. 4.** (a) The removal rate of TC by piezoelectric pipes. (b) Comparison of degradation efficiency of TC, RhB, CIP, and OTC. (c) Effect of water matrixes on TC degradation rate.

completely degraded, and the final degradation rate tended to be the same. To avoid the high flow rate greatly damaging or even washing away the catalyst on the inner wall of the pipe, considering the increase of flow will inevitably lead to an increase in pump energy consumption. Therefore, a low flow rate was selected for subsequent experiments.

The initial pH of 20 mg/L TC solutions was 6.45. Adding 0.5 M HCl or NaOH adjusted the pH to 2.16, 3.96, 8.25, and 10.05, respectively, to examine the effect of the initial pH on the degradation of TC in $Fe_3O_4$ @$MoS_2$/PVDF piezoelectric pipe. As shown in Fig. 5b, the strongly acidic environment (pH=2.16) was not conducive to the degradation reaction, which could be attributed to the reaction of the large number of $H^+$ and $e^-$ as shown in Eq. 4, inhibiting the formation of $\bullet O_2^-$, which reduced the number of active free radicals in the reaction, thus greatly reducing the degradation efficiency. When pH increased from 2.16 to 3.96, the removal rate increased by 11.37 %. The degradation rate reached 92.5 %, and the $k$ was 1.818 $mM^{-1}$ $min^{-1}$ at pH 6.45. However, at pH 8.25 and 10.05, the removal rate slowed down significantly, which may be because the alkaline environment was not conducive to a Fenton-like reaction [33], thus reducing the reaction rate.

The influences of coexisting anions ($Cl^-$, $CO_3^{2-}$ $NO_3^-$, and $SO_4^{2-}$) on TC degradation were investigated to analyze the stability of $Fe_3O_4$@$MoS_2$/PVDF piezoelectric pipe in natural water bodies. Different concentrations of $CO_3^{2-}$ and $Cl^-$ had different degrees of inhibition on TC degradation, as shown in Fig. 5c-f. There was little difference in the degradation efficiency at three diffident $Cl^-$ concentrations. However, the $k$ increased from 0.840 $mM^{-1}$ $min^{-1}$ to 1.261 $mM^{-1}$ $min^{-1}$ with the increase of $Cl^-$ from 50 to 100 mM (Fig. 5c). This was attributed to the generation of Cl• (Eqs. 5–6) which may be involved in the reaction. Fig. 5d indicated that $CO_3^{2-}$ had a significant inhibitory effect on degradation performance. On the one hand, $CO_3^{2-}$ was alkaline in the solution, $Mo^{4+}$ cannot be exposed on $Fe_3O_4$ @$MoS_2$/PVDF surfaces and $MoS_2$ had no activity under alkaline conditions [38]. On the other hand, $CO_3^{2-}$ acted as a scavenger to quench •OH (Eq. 7) and fewer reactive species were generated, which inhibited the piezocatalytic activity [39]. As shown in Fig. 5e, $NO_3^-$ had a strong promoting effect on TC degradation. The removal rate of TC reached 95.3 % ($NO_3^-$ at 10 mM) with the 5.454 $mM^{-1}$ $min^{-1}$ of $k$. With the increase of $NO_3^-$ concentration, its promoting effect weakens. Besides, different concentrations of $SO_4^{2-}$ had basically no effect on the TC removal rate (Fig. 5f). In conclusion, the $Fe_3O_4$@$MoS_2$/PVDF piezoelectric pipe can still maintain excellent piezocatalytic performance in a natural water environment, which has certain reference significance for practical application.

$$O_2 + 2H^+ + 2e^- \rightarrow H_2O_2 \quad (4)$$

$$Cl^- + \bullet OH \rightarrow ClOH^- \quad (5)$$

$$ClOH^- + H^+ \rightarrow H_2O + Cl\cdot \quad (6)$$

$$CO_3^{2-} + \bullet OH \rightarrow CO_3^{\bullet -} + OH^- \quad (7)$$

To test whether the intermittent impact and the constant current delivery of the peristaltic has an effect on degradation performance, the peristaltic pump used in this work and a centrifugal pump (RGP-30 Kunshan Olanke Pump Manufacturing Co., LTD.) were selected to transport the pollutant solution. Both pumps were tested at four flow rates. As shown in Fig. 6a-b, driven by peristaltic pump, TC degradation rates at 0.15, 0.30, 0.40 and 0.60 L $min^{-1}$ were 92.8 %, 93.1 %, 94.6 % and 96.2 %, respectively. The removal rates driven by the centrifugal pump were 82.7 %, 88.6 %, 93.5 % and 94.2 % respectively. The results showed that the degradation rate of the two pump systems increased with the increase of the flow rate. At the same flow rate, the degradation performance of peristaltic pump was higher than that of centrifugal pump, indicating that the flow pulse induced by peristaltic pump can better improve the piezoelectric response of catalyst.

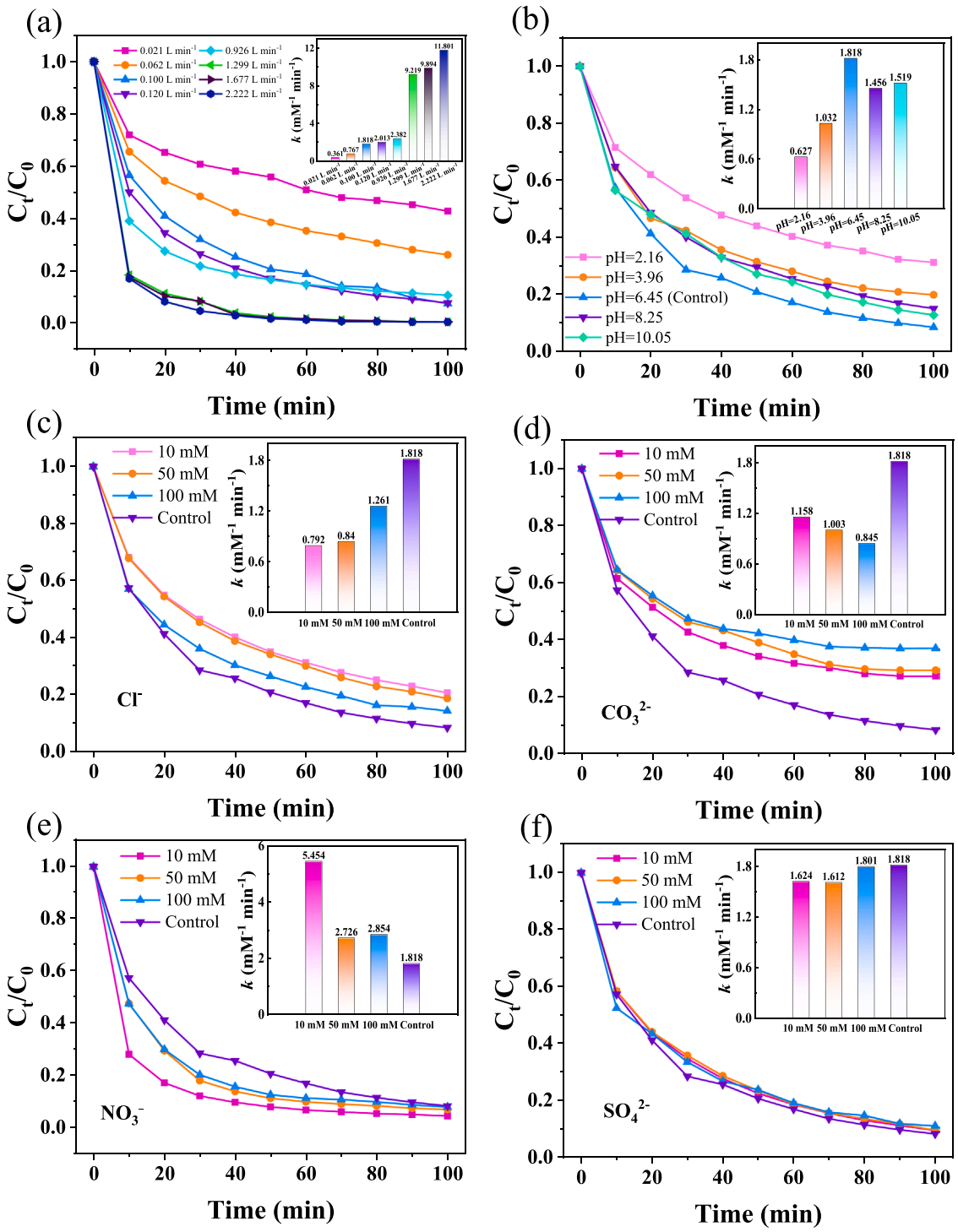


**Fig. 5.** Effects of (a) flow rate, (b) initial pH and coexisting anions (c) $Cl^-$, (d) $CO_3^{2-}$, (e) $NO_3^-$ and (f) $SO_4^{2-}$ on TC degradation and the corresponding apparent second-order rate constants.

### 3.5. The energy consumption

With the decrease in global energy, energy consumption has been part of the key issues in the field of catalysis. Compared with photocatalytic technology, piezocatalysis is characterized by low energy consumption due to its use of mechanical energy in nature such as water flow to degrade pollutants. EE/O (kWh $m^{-3}$ $order^{-1}$) proposed by the International Union of Pure and Applied Chemistry is used to calculate the energy required for pollutant degradation [40]. Table 1 listed the energy consumption of different piezocatalysis processes (the calculation formula was shown in Text S3), which displayed that the EE/O value of pollutant degradation driven by visible light irradiation, ultrasonic, and ball milling varied from 935.33 to 43066.67 kWh $m^{-3}$ $order^{-1}$, while the EE/O value of self-powered water flow piezocatalytic system was only 241.04 kWh $m^{-3}$ $order^{-1}$. The calculation formula of the pseudo-first-order rate constant $k$ is shown in Eq. S4 in the Supporting information. Therefore, the $Fe_3O_4$ @$MoS_2$/PVDF pipe used in this study had the characteristics of low energy consumption and may be more suitable for pollutant degradation.

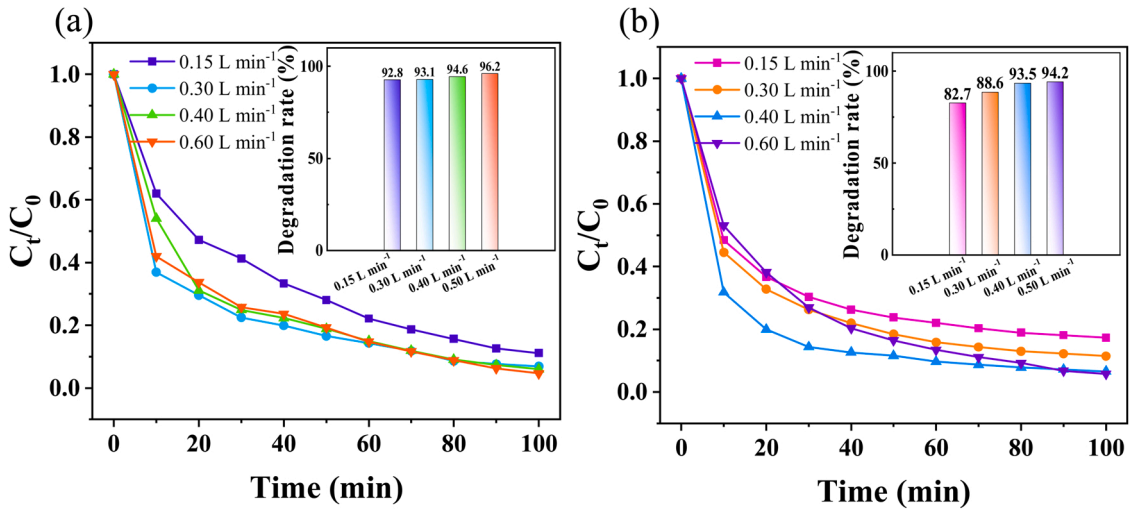


**Fig. 6.** Comparison of TC removal rates under (a) peristaltic pump and (b) centrifugal pump.

**Table 1**
Comparison of energy consumption of the different catalytic systems.

| Material | Pollutant | Driving force | Amount of catalyst (mg) | Pollutants concentration (mg/L) / Wastewater volume (mL) | Degradation efficiency/ Reaction time (min) | $k$ ($\times 10^{-3}$ $min^{-1}$) | P (kW) | EE/O (kWh $m^{-3}$ $order^{-1}$) | Ref. |
|---|---|---|---|---|---|---|---|---|---|
| $MoS_2$ NTs/ $CuInS_2$ QDs | Tetracycline | visible-light | 10 | 30 / 60 | 89.0 % / 180 | 12.0 | 0.300 | 16150.00 | [41] |
| $Sn_3O_4$/g-$C_3N_4$ | Ciprofloxacin | visible light | 25 | 10 / 100 | 26.5 % / 120 | 2.7 | 0.300 | 43066.67 | [42] |
| $Bi_4Ti_3O_{12}$ | Tetracycline | ultrasonic | 100 | 10 / 100 | 82.0 % / 150 | 10.8 | 0.180 | 6460.00 | [43] |
| $K_2Ti_6O_{13}$/$TiO_2$ | Tetracycline | ultrasonic | 50 | 50 / 50 | ~54.0 % / 120 | 24.0 | 0.160 | 5168.00 | [44] |
| $Cu_2O$/$MoS_2$/rGO | Tetracycline | ultrasonic | 30 | 20 / 100 | 66.0 % / 75 | 18.0 | 0.120 | 2584.00 | [45] |
| | Ciprofloxacin | ultrasonic | 30 | 10 / 100 | 31.8 % / 90 | 6.0 | 0.120 | 7752.00 | |
| E-$MoS_2$/PVDF | Oxytetracycline | ultrasonic | 100 | 20 / 100 | 93.08 % / 24 | 91.2 | 0.650 | 2762.50 | [22] |
| $MoS_2$ | Tetracycline | ultrasonic | 10 | 4.4 / 100 | 93.0 % / 120 | 22.5 | 0.110 | 1894.93 | [13] |
| $Fe_3O_4$@$MoS_2$ | Rhodamine B | ultrasonic | 30 | 40 / 30 | ~90.0 % / 60 | 19.0 | 0.250 | 17000.00 | [46] |
| Ag/$PbBiO_2I$ | Rhodamine B | ultrasonic | 100 | 10 / 100 | ~85.0 % / 90 | 16.5 | 0.120 | 2818.91 | [47] |
| $MoS_2$/GDY | Tetracycline | ball milling | 40 | 100 / 50 | 92.2 % / 40 | 51.8 | 0.250 | 935.33 | [48] |
| $BaTiO_3$ +PMS | Carbamazepine | water flow | 100 | $1.98 \times 10^{-3}$ / 10 | 76.2 % / 80 | 8.15 | $6.66 \times 10^{-6}$ | 428.65 | [40] |
| $BaTiO_3$-$TiO_2$ nanofibers | Rhodamine B | water flow | 10 | 10 / 100 | 99.8 % / 60 | 59.4 | 0.300 | 1957.58 | [49] |
| $Fe_3O_4$@$MoS_2$/ PVDF pipe | Tetracycline | water flow | 200 | 20 / 200 | 91.5 % / 100 | 20.1 | 0.025 | 241.04 | This work |

### 3.6. Stability study

In order to examine the stability of $Fe_3O_4$ @$MoS_2$/PVDF piezoelectric pipe, the cyclic degradation of TC was carried out. As shown in Fig. 7a, the removal rate of TC was reduced to 75.3 %. According to the comparison of SEM images of $Fe_3O_4$ @$MoS_2$/PVDF sample before the reaction (Fig. 7b) and after the cycling experiment (Fig. 7c), it can be seen that under the impact of water flow for a long time, there are obvious tears and fouling structures on the surface of $Fe_3O_4$ @$MoS_2$/PVDF. Therefore, it was speculated that the decrease in stability and degradation efficiency was due to the loss of $Fe_3O_4$@$MoS_2$ on the PVDF substrate [50–52]. To explore the effect of pH conditions on stability, the initial pH of TC was adjusted to 2, 5, 8 and 11 respectively, and then the cyclic degradation experiment was carried out. As shown in Fig. S6, it can be seen that the degradation performance of $Fe_3O_4$@$MoS_2$/PVDF pipe under pH 2, 5, 8 and 11 basically showed a trend of decreasing gradually with the increase of the times of use. At pH = 2, the degradation rate was not ideal because of the large number of competitive reactions between $H^+$ and $e^-$ (Eq. 4). When pH = 5, the removal rate of TC remains at the highest level. Combined with the experimental results of pH influence, it can be concluded that pH = 5–6.45 was the best pH range for TC degradation of $Fe_3O_4$@$MoS_2$/PVDF piezoelectric pipe. However, under alkaline conditions (pH = 8 and 11), the degradation rate also decreased gradually, because alkaline conditions were not conducive to Fenton-like reaction [33], so the reaction activity is inhibited. In summary, the reusability of $Fe_3O_4$@$MoS_2$/PVDF piezoelectric pipe for TC degradation cannot be ignored due to the influence of pH, and its stability at different pH remains to be studied and improved.

### 3.7. Piezocatalytic mechanism

The mechanism of piezoelectric degradation of TC by $Fe_3O_4$ @$MoS_2$/PVDF piezoelectric pipe was analyzed by active species trapping experiments. EDTA-2Na, TBA and p-BQ [49] were used as scavengers for hole ($h^+$), hydroxyl (•OH), and superoxide radical ($\bullet O_2^-$), respectively, to determine the types of active radicals, because they correspond to large second order rate constants, $k$ (TBA, •OH) = 3.8 ~ 7.6 × $10^8$ $M^{-1}$ $s^{-1}$, $k$ (p-BQ, $\bullet O_2^-$) = 0.9 ~ 1.0 × $10^9$ $M^{-1}$ $s^{-1}$ [53]. As shown in Fig. 8a, when •OH was captured by TBA, the degradation efficiency of TC decreased by 34.9 %. In the presence of p-BQ and EDTA, the removal rates of TC decreased from 92.5 % to 60.2 % and 36.5 %, respectively, indicating

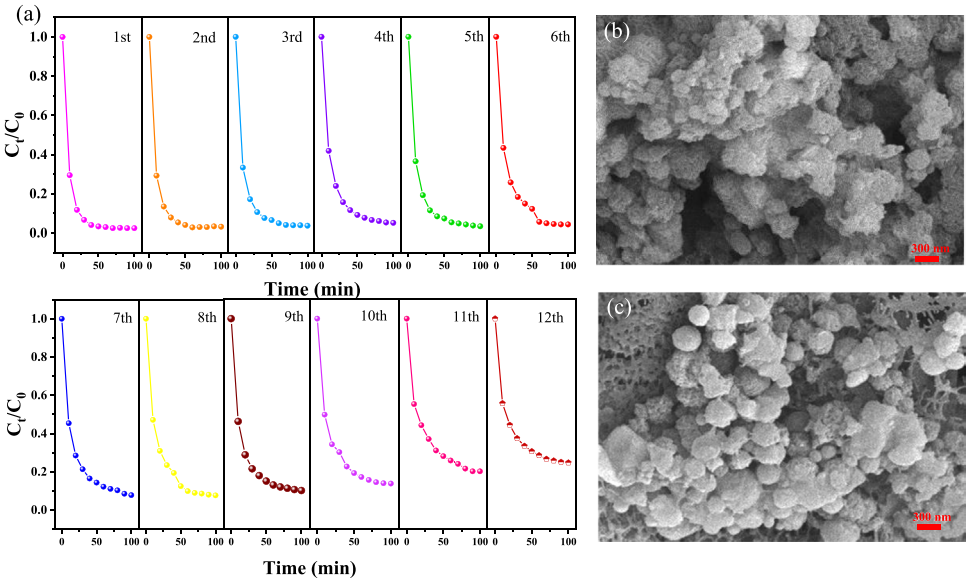


**Fig. 7.** (a) Cyclical tests. SEM images of $Fe_3O_4$@$MoS_2$/PVDF (b) before and (c) after the reaction.

that •OH, $\bullet O_2^-$ and $h^+$ all played a role in the degradation of TC. In addition, EPR experiments were conducted to further verify the existence of these radicals. As shown in Fig. 8b, TEMPO-$h^+$ signals with 1:1:1 intensity can be observed, indicating the generation of $h^+$. Due to the neutralization of TEMPO on $h^+$ [54,55], the intensity of TEMPO-$h^+$ signal decreased from $2.1 \times 10^5$ a.u. at the initial moment to $1.3 \times 10^5$ a.u. As shown in Fig. 8c-d, there were sixfold peak and standard equidistant quadruple peak signals with a peak of 1:2:2:1, which were typical EPR spectrum of DMPO-$\bullet O_2^-$and DMPO-•OH [56], respectively. The DMPO-$\bullet O_2^-$ signal increased from $2.0 \times 10^4$ a.u. to $3.5 \times 10^4$ a.u. over time. Similarly, the DMPO-•OH signal also showed an increase in intensity from $1.0 \times 10^4$ a.u. to $2.1 \times 10^4$ a.u., indicating the rapid generation and continuous accumulation of $\bullet O_2^-$ and •OH. The results of EPR were consistent with those of the radicals trapping experiment, and the generation of •OH, $\bullet O_2^-$, and $h^+$ played an important role in piezocatalysis.

According to the generation of •OH, $\bullet O_2^-$, and $h^+$ during degradation, the possible mechanism of radicals' formation was proposed, as shown in Fig. 8e. When $Fe_3O_4$ and $MoS_2$ contacted and formed heterostructures at the interface, band bending will occur, leading to charge transfer and separation [57–59]. Because the conduction band CB of $MoS_2$ was higher than that of $Fe_3O_4$, the $e^-$ in the CB of $MoS_2$ was transferred to the CB of $Fe_3O_4$, leaving $h^+$ in the valence band (VB) [60]. The driving force of water flow caused polarization deformation and induced the generation of the internal electric field. In addition, the coupling of $Fe_3O_4$@$MoS_2$ and PVDF effectively improved the separation of $e^-$ and $h^+$, and then migrated to the surface of the catalysts. $\bullet O_2^-$ was formed by the redox reaction of $O_2$ and $e^-$, and •OH was formed by the redox reaction of $H_2O$ and $h^+$, the generated •OH, $\bullet O_2^-$, and $h^+$ served as oxidation active species to degrade TC [61].

In order to elucidate the formation of active radicals, main reactions and the causes of catalyst deactivation in piezocatalysis. XPS was used to characterize the valence distribution of $Fe_3O_4$@$MoS_2$/PVDF after 1 and 5 cycles. As shown in Fig. S7, the contents of $Mo^{4+}$ and $Fe^{3+}$ in the catalyst decreased by about 2.6 % and 5.6 %, while the contents of $Mo^{6+}$ and $Fe^{2+}$ increased by about 21.6 % and 26.8 %, respectively. It has been reported that $MoS_2$ can be used as a cocatalyst to enhance the $Fe^{2+}/Fe^{3+}$ cycle and accelerate the generation of reactive species [62]. In addition, $Mo^{4+}$ was oxidized to a high valence state and cannot continue to participate in the reduction of $Fe^{3+}$, so the reactivity was irreversibly reduced [63–65]. As shown in Fig. S7c, the content of $S^{2-}$ was reduced by 2.2 %, while the content of $S_1$ after oxidation was increased by 37.5 %, which proved that $S^{2-}$ was irreversibly oxidized to a high valence state in the reaction process. In addition, unsaturated sulfur binds to the surface of $MoS_2$ and was easily released with the aid of proton binding. This reducing sulfide can assist in electron transfer. However, this does not occur once the unsaturated sulfur is irreversibly depleted [32,63]. Fig. S7c showed that the unsaturated sulfur content was reduced by 9.3 %. Therefore, it is not conducive to the electron transfer in the catalytic reaction, and thus the reaction activity was reduced. It can be concluded that another reason for the partial deactivation in the cycling experiment was due to the decrease of active sites $Fe^{3+}$ and $Mo^{4+}$ and the loss of partial unsaturated sulfur.

### 3.8. Degradation pathway

In order to further clarify the reaction mechanism of TC degradation, the intermediates with different reaction times in $Fe_3O_4$@$MoS_2$/PVDF piezoelectric pipe system were identified by LC-MS. More information about the structure and molecular formula of the intermediates is listed in Table S3. The Fukui index has been used to predict electrophilic, nucleophilic, and radical attack sites in organic molecules [65,66]. Among them, the f(0) values of C15, C17, O22, and N27 were larger than those of similar atoms, indicating that they were vulnerable to free radical attack [67] (Table S4). In addition, chemical reactions were often accompanied by electron transfer. Based on the frontier orbital theory, higher HOMO energy indicated a stronger electron-giving capacity, while a lower LUMO energy indicated a stronger electron-receiving capacity [68]. The optimized structure of TC was shown in Fig. 9a. Sites with high electron density (such as N27, C16, C17, C29, C28, O26, C13, and C18) were vulnerable to electrophilic attack (Fig. 9b), while sites C15, C17, O22, C7, and C11 on the molecule were vulnerable to nucleophilic attack (Fig. 9c) [69].

Based on LC-MS results and Fukui index, possible degradation pathways of TC were proposed, as shown in Fig. 9d. In pathway 1, the TC molecule was attacked by •OH and $\bullet O_2^-$ and hydroxylated to form intermediate P1 ($m/z = 461$) [70]. P1 had two degradation pathways: one was that P2 ($m/z = 432$) was formed through oxidation and deamination, and then intermediate P4 ($m/z = 349$), P6 ($m/z = 305$), and P8 ($m/z = 261$) were successively formed through further oxidation and ring-opening reactions. The other was further hydroxylation to form P3 ($m/z = 476$) because there were double bonds and groups with high electron density in TC molecules, which were vulnerable to free radical attack [71,72]. After the dehydroxylation of P3 to P5 ($m/z = 459$), P6

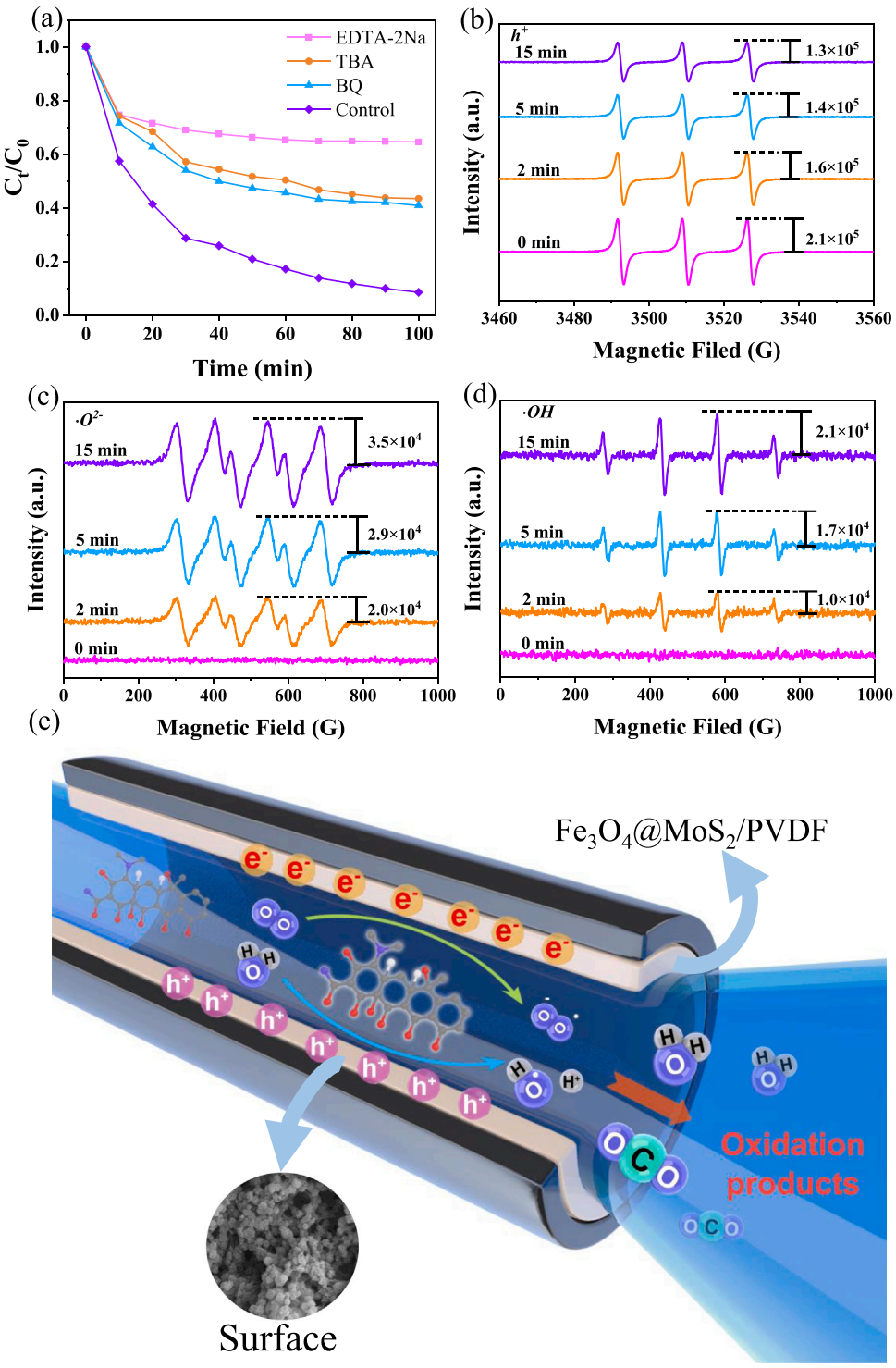


**Fig. 8.** (a) Active species scavenging experiment. (b) EPR spectra of $h^+$ by TEMPO, (c) $\bullet O_2^-$ by DMPO, and (d) •OH by DMPO. (e) Mechanism of TC removal by $Fe_3O_4$@$MoS_2$/PVDF piezoelectric pipe.

($m/z = 305$), P7 ($m/z = 353$), and P8 ($m/z = 261$) were obtained through a series of reactions including demethylation, ring-opening, C-N bond cleavage and oxidation at C18, and deamidation at C16. In pathway 2, the TC molecule was demethylated to form P9 ($m/z = 416$), then closed amino and amide groups, forming intermediate P10 ($m/z = 358$), which was cleaved to obtain P11 ($m/z = 306$), and then P11 closed two methyl groups to obtain P12 ($m/z = 278$). Further ring-opening decomposition to form P13 ($m/z$ 246). •OH and $\bullet O_2^-$ further interacted with these intermediates, leading to ring destruction and thus to the formation of $CO_2$ and $H_2O$ through an oxidation process.

### 3.9. Toxicity assessment

The release of metal ions from nanomaterials in water environment may lead to potential biological toxicity. It is necessary to assess the toxicity of Mo and Fe ions released from the TC degraded solution. ICP-MS technology was used to detect the sample solution, and the results were shown in Table S1 and Table S2. According to the test results and

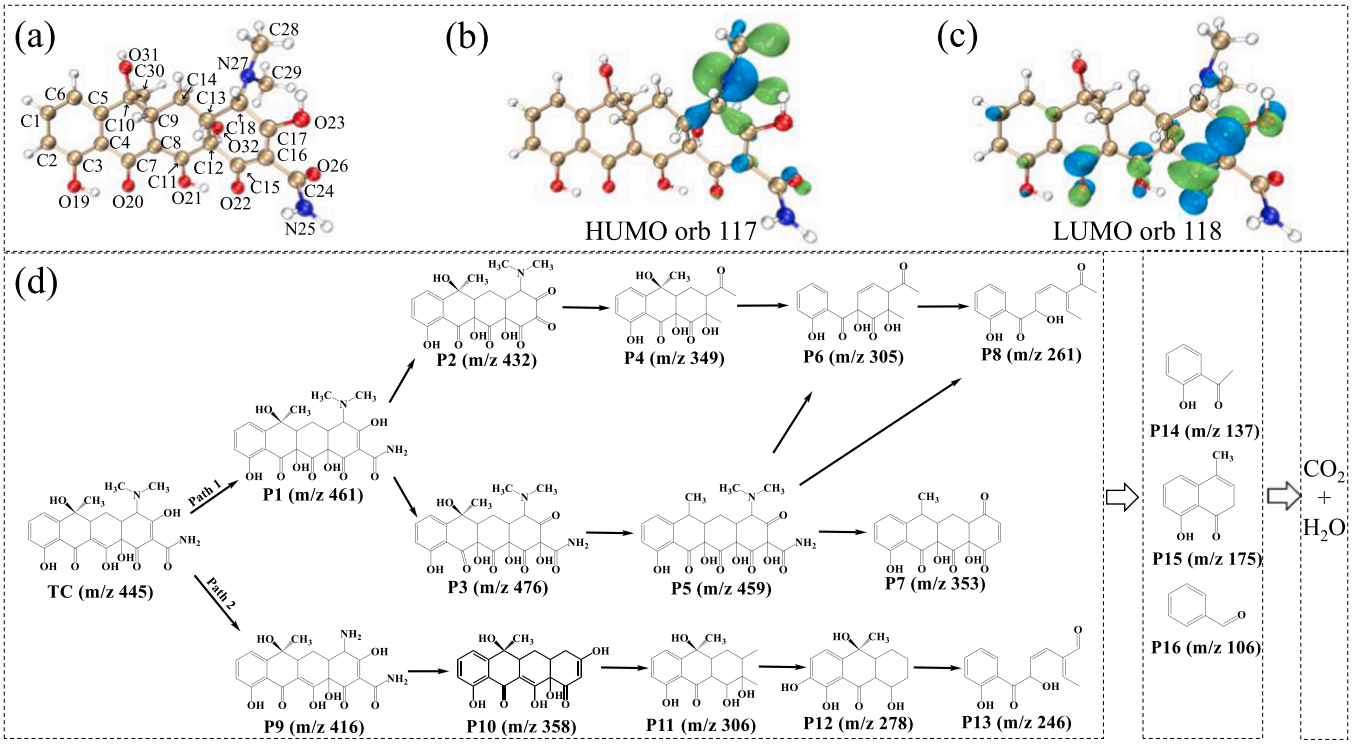


**Fig. 9.** (a) Optimized structure. (b) Fukui index. (c) HOMO and LUMO of TC. (d) Possible TC degradation pathways.

calculation, the content of Mo and Fe ions released into TC wastewater only accounted for 1.90 % and 1.16 % of the amount of $Fe_3O_4$ @$MoS_2$ catalyst, respectively. In order to obtain the toxicity level of the intermediates, toxicity estimation software (T.E.S.T.) [64,73] based on the quantitative structure-activity relationship (QSAR) model was used to estimate the ecotoxicity of TC and its intermediates. The relevant

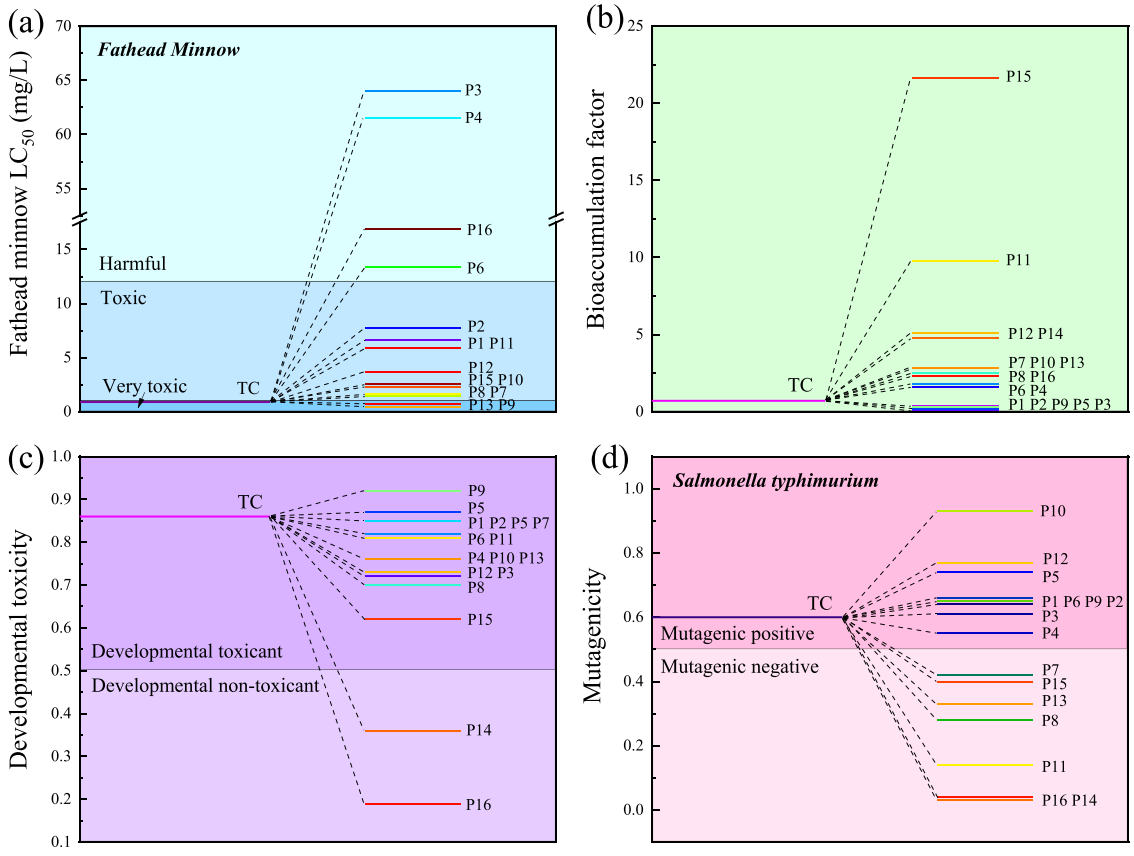


**Fig. 10.** (a) Acute toxicity. (b) bioaccumulation factor. (c) developmental toxicity, and (d) mutagenicity of parent TC and intermediates.

information was shown in Text S4 and the related data were summarized in Table S3. Because the organic pollutant wastewater had the most direct impact on aquatic organisms, Fathead minnow $LC_{50}$ was only selected as acute toxicity for a detailed description. The $LC_{50}$ of TC was 0.9 mg/L, which was "very toxic". Among all intermediates, P9 showed the highest acute toxicity ($LC_{50}$ = 0.47 mg/L) (Fig. 10a). The intermediate P13 also showed high acute toxicity ($LC_{50}$ = 0.74 mg/L). The acute toxicity of the remaining intermediates was lower than that of TC, but P1, P2, P7, P8, P11, P12, and P15 were still considered "toxic". Intermediates P3, P4, P6, and P16 ($LC_{50}$ of 64.04, 61.56, 22.75, and 16.87 mg/L, respectively) were significantly reduced to harmful levels due to ring opening and hydroxylation. The bioaccumulation factors (BCF) of P1, P2, P3, P5, and P9 were 0.36, 0.3, 0.09, 0.17, and 0.29, respectively, as shown in Fig. 10b, which were significantly lower than TC (BCF=0.71), indicating that their bioaccumulation potential was significantly reduced. However, the bioaccumulation factors of the remaining intermediates were higher than TC, especially P11 (BCF=9.80) and P15 (BCF=21.66). As shown in Fig. 10c, TC was classified as a developmental toxic substance that interferes with the development of the organism during the embryonic stage. Other intermediates fluctuated within the developmental toxic range, but P14 and P16 were considered "developmental non-toxic". In addition, TC was mutagenic positive, but after degradation, nearly half of the intermediates were "mutagenic negative" (Fig. 10d). In general, QSAR prediction demonstrated that $Fe_3O_4$@$MoS_2$/PVDF pipe piezoelectric catalytic degradation of TC in this study had a significant effect on eliminating ecotoxicity.

## 4. Conclusion

A novel self-powered $Fe_3O_4$@$MoS_2$/PVDF piezoelectric pipe was prepared. The driving force generated by the continuous water flow in the pipe system deformed $Fe_3O_4$@$MoS_2$/PVDF, resulting in piezoelectric polarization at its active site and the generation of $h^+$, •OH, and $•O_2^-$ for efficient piezocatalytic decomposition of organic pollutants. Theoretical simulation and calculation showed that $Fe_3O_4$@$MoS_2$/PVDF piezoelectric pipe had excellent piezocatalytic performance. TC, RhB, CIP, and OTC were degraded by 92.5 %, 90.9 %, 85.9 %, and 69.2 % within 100 min, respectively, and the ecological toxicity of most intermediates was reduced or even eliminated, indicating that the environmental impact of intermediates could be reduced. After 12 cycles, the removal rate of TC was still 75.3 %, which had excellent reusability and strong adaptability to different influencing factors. Most importantly, the $Fe_3O_4$@$MoS_2$/PVDF piezoelectric pipe system has an extremely low energy consumption compared to traditional ultrasonic processes. This work can provide a promising method for the removal of organic pollutants by using natural water flow and may have important guidance for the efficient environmentally friendly degradation of organics in water.

## CRediT authorship contribution statement

**Jingxue Wang:** Conceptualization, Methodology, Formal analysis, Writing – original draft. **Xiaonan Zhou:** Investigation, methodology, Writing – review & editing. **Juncheng Hao:** Resources, Writing – review & editing, Supervision. **Zichen Wang:** Methodology, Writing – review & editing. **Bingjie Huo:** Methodology, Investigation. **Jianguang Qi:** Supervision, Writing – review & editing. **Yinglong Wang:** Supervision, Writing – review & editing. **Fanqing Meng:** Conceptualization, Funding acquisition, Supervision, Writing – review & editing.

## Declaration of Competing Interest

The authors declare that they have no known competing financial interests or personal relationships that could have appeared to influence the work reported in this paper.

## Data Availability

No data was used for the research described in the article.

## Acknowledgements

We are grateful for the financial support from the Natural Science Foundation of Shandong Province [ZR2020QB144].

## Appendix A. Supporting information

Supplementary data associated with this article can be found in the online version at doi:10.1016/j.apcatb.2023.122655.

## References

[1] H.B. Gu, W.H. Xie, A. Du, D. Pan, Z.H. Guo, Overview of electrocatalytic treatment of antibiotic pollutants in wastewater, Catal. Rev. (2021) 1–51, https://doi.org/10.1080/01614940.2021.1960009.
[2] M. Shigei, A. Assayed, A. Hazaymeh, S.S. Dalahmeh, Pharmaceutical and Antibiotic Pollutant Levels in Wastewater and the Waters of the Zarqa River, Jordan, Appl. Sci. 11 (2021) 8638, https://doi.org/10.3390/app11188638.
[3] C. Monahan, S. Harris, D. Morris, E. Cummins, A comparative risk ranking of antibiotic pollution from human and veterinary antibiotic usage – an Irish case study, Sci. Total Environ. 826 (2022), 154008, https://doi.org/10.1016/j.scitotenv.2022.154008.
[4] Y.X. Zhang, J.H. Wang, J. Lu, J. Wu, Antibiotic resistance genes might serve as new indicators for wastewater contamination of coastal waters: Spatial distribution and source apportionment of antibiotic resistance genes in a coastal bay, Ecol. Indic. 114 (2020), 106299, https://doi.org/10.1016/j.ecolind.2020.106299.
[5] J.L. Wang, L.B. Chu, L. Wojnárovits, E. Takács, Occurrence and fate of antibiotics, antibiotic resistant genes (ARGs) and antibiotic resistant bacteria (ARB) in municipal wastewater treatment plant: an overview, Sci. Total Environ. 744 (2020), 140997, https://doi.org/10.1016/j.scitotenv.2020.140997.
[6] X.E. Ning, A.Z. Hao, Y.L. Cao, J.D. Hu, J. Xie, D.Z. Jia, Effective promoting piezocatalytic property of zinc oxide for degradation of organic pollutants and insight into piezocatalytic mechanism, J. Colloid Interface Sci. 577 (2020) 290–299, https://doi.org/10.1016/j.jcis.2020.05.082.
[7] J.J. Long, T.T. Ren, J. Han, N.J. Li, D.Y. Chen, Q.F. Xu, H. Li, J.M. Lu, Heterostructured $BiFeO_3$@CdS nanofibers with enhanced piezoelectric response for efficient piezocatalytic degradation of organic pollutants, Sep. Purif. Technol. 290 (2022), 120861, https://doi.org/10.1016/j.seppur.2022.120861.
[8] T.T. Ren, W.R. Tian, Q. Shen, Z.T. Yuan, D.Y. Chen, N.J. Li, J.M. Lu, Enhanced piezocatalysis of polymorphic few-layered $MoS_2$ nanosheets by phase engineering, Nano Energy 90 (2021), 106527, https://doi.org/10.1016/j.nanoen.2021.106527.
[9] Y. Wei, Y.W. Zhang, W. Geng, H.R. Su, Efficient bifunctional piezocatalysis of Au/$BiVO_4$ for simultaneous removal of 4-chlorophenol and Cr(VI) in water, Appl. Catal. B 259 (2019), 118084, https://doi.org/10.1016/j.apcatb.2019.118084.
[10] Z.J. Wang, B.J. Huo, J.W. Wang, W. Ma, J.G. Qi, Z.Y. Zhu, F.Q. Meng, Y.L. Wang, In situ synthesis of flower-structured ZnO@YFC for the efficient piezocatalytic degradation of tetracycline wastewater: Degradation mechanism and toxicity evolution, Appl. Surf. Sci. 602 (2022), 154330, https://doi.org/10.1016/j.apsusc.2022.154330.
[11] H.Y. Lin, K.T. Le, P.H. Chen, J.M. Wu, Systematic investigation of the piezocatalysis–adsorption duality of polymorphic $MoS_2$ nanoflowers, Appl. Catal. B 317 (2022), 121717, https://doi.org/10.1016/j.apcatb.2022.121717.
[12] G. Nie, L. Xiao, J.X. Bi, S.B. Wang, New insight to piezocatalytic peroxymonosulfate activation: The critical role of dissolved oxygen in mediating radical and nonradical pathways, Appl. Catal. B 315 (2022), 121584, https://doi.org/10.1016/j.apcatb.2022.121584.
[13] S. Li, Z.C. Zhao, D.F. Yu, J.Z. Zhao, Y.P. Su, Y. Liu, Y.H. Lin, W.S. Liu, H. Xu, Z. T. Zhang, Few-layer transition metal dichalcogenides ($MoS_2$, $WS_2$, and $WSe_2$) for water splitting and degradation of organic pollutants: understanding the piezocatalytic effect, Nano Energy 66 (2019), 104083, https://doi.org/10.1016/j.nanoen.2019.104083.
[14] F.Q. Meng, W. Ma, Y.L. Wang, Z.Y. Zhu, Z. Chen, G. Lu, A tribo-positive Fe@$MoS_2$ piezocatalyst for the durable degradation of tetracycline: degradation mechanism and toxicity assessment, Environ. Sci.: Nano 7 (2020) 1704–1718, https://doi.org/10.1039/D0EN00284D.
[15] B.J. Huo, F.Q. Meng, J.W. Yang, Y.L. Wang, J.G. Qi, W. Ma, Z.C. Wang, J.X. Wang, Z.C. Wang, High efficiently piezocatalysis degradation of tetracycline by few-layered $MoS_2$/GDY: mechanism and toxicity evaluation, Chem. Eng. J. 436 (2022), 135173, https://doi.org/10.1016/j.cej.2022.135173.
[16] Q.W. Wang, S.Y. Dong, D. Zhang, C.F. Yu, J. Lu, D. Wang, J.H. Sun, Magnetically recyclable visible-light-responsive $MoS_2$@$Fe_3O_4$ photocatalysts targeting efficient wastewater treatment, J. Mater. Sci. 53 (2017) 1–13, https://doi.org/10.1007/s10853-017-1608-2.
[17] H.H. Singh, N. Khare, Flexible ZnO-PVDF/PTFE based piezo-tribo hybrid nanogenerator, Nano Energy 51 (2018) 216–222, https://doi.org/10.1016/j.nanoen.2018.06.055.

[18] L.C. Wan, W.R. Tian, N.J. Li, D.Y. Chen, Q.F. Xu, H. Li, J.H. He, J.M. Lu, Hydrophilic porous PVDF membrane embedded with $BaTiO_3$ featuring controlled oxygen vacancies for piezocatalytic water cleaning, Nano Energy 94 (2022), 106930, https://doi.org/10.1016/j.nanoen.2022.106930.

[19] G. Singh, M. Sharma, R. Vaish, Flexible Ag@$LiNbO_3$/PVDF composite film for piezocatalytic dye/pharmaceutical degradation and bacterial disinfection, ACS Appl. Mater. Interfaces 13 (2021) 22914–22925, https://doi.org/10.1021/acsami.1c01314.

[20] J. Wu, N. Qin, D.H. Bao, Effective enhancement of piezocatalytic activity of $BaTiO_3$ nanowires under ultrasonic vibration, Nano Energy 45 (2018) 44–51, https://doi.org/10.1016/j.nanoen.2017.12.034.

[21] S.T. Gao, H.J. Xing, J.J. Zhang, Y.P. Liu, H.W. Du, Z.J. Zhu, J.Y. Wang, X. Li, S. W. Zhang, Y.X. Yao, L.L. Ren, Oxalic acid functionalization of $BaTiO_3$ nanobelts for promoting their piezo-degradation organic contaminants, J. Mater. 7 (2021) 1275–1283, https://doi.org/10.1016/j.jmat.2021.03.002.

[22] W. Ma, B.H. Yao, W. Zhang, Y.Q. He, Y. Yu, J.F. Niu, Fabrication of PVDF-based piezocatalytic active membrane with enhanced oxytetracycline degradation efficiency through embedding few-layer E-$MoS_2$ nanosheets, Chem. Eng. J. 415 (2021), 129000, https://doi.org/10.1016/j.cej.2021.129000.

[23] Y. Tang, X.Q. Chen, M.D. Zhu, X.M. Liao, S. Hou, Y. Yu, X.Y. Fan, The strong alternating built-in electric field sourced by ball milling on $Pb_2BO_3X$ (X=Cl, Br, I) piezoelectric materials contributes to high catalytic activity, Nano Energy 101 (2022), 107545, https://doi.org/10.1016/j.nanoen.2022.107545.

[24] H.J. Li, Y. Xiong, Y.M. Wang, W.M. Ma, J.P. Fang, X. Li, Y. Qi. Han, C.Q. Liu, P. F. He, Fang, High piezocatalytic capability in CuS/$MoS_2$ nanocomposites using mechanical energy for degrading pollutants, J. Colloid Interface Sci. 609 (2022) 657–666, https://doi.org/10.1016/j.jcis.2021.11.070.

[25] J. Lu, Y. Zhou, Y.B. Zhou, Efficiently activate peroxymonosulfate by $Fe_3O_4$@$MoS_2$ for rapid degradation of sulfonamides, Chem. Eng. J. 422 (2021), 130126, https://doi.org/10.1016/j.cej.2021.130126.

[26] T. Lu, F.W. Chen, Multiwfn: a multifunctional wavefunction analyzer, J. Comput. Chem. 33 (2012) 580–592, https://doi.org/10.1002/jcc.22885.

[27] T. Lu, Q.X. Chen, mwfn: a strict, concise and extensible format for electronic wavefunction storage and exchange, ChemRxiv (2020), https://doi.org/10.26434/chemrxiv-2021-lt04f-v5.

[28] X.L. Xu, X.J. Liu, J.Y. Xu, J.Z. Zhou, X. Sun, D. Wu, C.W. Zhang, X. Ren, Q. Wei, Interface engineering of $Fe_3O_4$@$MoS_2$ nanocomposites: high efficiency electrocatalytic synthesis of $NH_3$ under mild conditions, Chem. Eng. J. 437 (2022), 135417, https://doi.org/10.1016/j.cej.2022.135417.

[29] M.N. Chai, W.S. Tong, Z.H. Wang, Z.S. Chen, Y.C. An, Y.H. Zhang, Piezoelectric-Fenton degradation and mechanism study of $Fe_2O_3$/PVDF-HFP porous film drove by flowing water, J. Hazard. Mater. 430 (2022), 128446, https://doi.org/10.1016/j.jhazmat.2022.128446.

[30] Y. Zhou, L. Zhou, Y.B. Zhou, M.Y. Xing, J.L. Zhang, Z-scheme photo-Fenton system for efficiency synchronous oxidation of organic contaminants and reduction of metal ions, Appl. Catal. B 279 (2020), 119365, https://doi.org/10.1016/j.apcatb.2020.119365.

[31] K.Y. Qi, Z.M. Yuan, Y. Hou, R.C. Zhao, B.W. Zhang, Facile synthesis and improved Li-storage performance of Fe-doped $MoS_2$/reduced graphene oxide as anode materials, Appl. Surf. Sci. 483 (2019) 688–695, https://doi.org/10.1016/j.apsusc.2019.04.021.

[32] R. Bai, W.F. Yan, Y. Xiao, S.Q. Wang, X.C. Tian, J.P. Li, X.F. Xiao, X.Q. Lu, F. Zhao, Acceleration of peroxymonosulfate decomposition by a magnetic $MoS_2$/$CuFe_2O_4$ heterogeneous catalyst for rapid degradation of fluoxetine, Chem. Eng. J. 397 (2020), 125501, https://doi.org/10.1016/j.cej.2020.125501.

[33] J.D. Lu, The effect of two ferromagnetic metal stripes on valley polarization of electrons in a graphene, Phys. Lett. A 384 (2020), 126402, https://doi.org/10.1016/j.physleta.2020.126402.

[34] X. Liu, M.Y. Deng, X.H. Wang, Nanoscale domain imaging and local piezoelectric coefficient $d_{33}$ studies of single piezoelectric polymeric nanofibers, Mater. Lett. 189 (2017) 66–69, https://doi.org/10.1016/j.matlet.2016.11.044.

[35] J.H. Lin, Y.H. Tsao, M.H. Wu, T.M. Chou, Z.H. Lin, J.M. Wu, Single- and few-layers $MoS_2$ nanocomposite as piezo-catalyst in dark and self-powered active sensor, Nano Energy 31 (2017) 575–581, https://doi.org/10.1016/j.nanoen.2016.12.013.

[36] Y. Xue, P.F. Wang, C. Wang, Y.H. Ao, Efficient degradation of atrazine by BiOBr/UiO-66 composite photocatalyst under visible light irradiation: Environmental factors, mechanisms and degradation pathways, Chemosphere 203 (2018) 497–505, https://doi.org/10.1016/j.chemosphere.2018.04.017.

[37] H.N. Wang, C.J. Zhang, F.H. Rana, Ultrafast dynamics of defect-assisted electron–hole recombination in monolayer $MoS_2$, Nano Lett. 15 (2015) 339–345, https://doi.org/10.1021/nl503636c.

[38] B. Sheng, F. Yang, Y.H. Wang, Z.H. Wang, Q. Li, Y.G. Guo, X.Y. Lou, J.S. Liu, Pivotal roles of $MoS_2$ in boosting catalytic degradation of aqueous organic pollutants by Fe(II)/PMS, Chem. Eng. J. 375 (2019), 121989, https://doi.org/10.1016/j.cej.2019.121989.

[39] L.M. Hu, G.S. Zhang, M. Liu, Q. Wang, P. Wang, Enhanced degradation of Bisphenol A (BPA) by peroxymonosulfate with $Co_3O_4$-$Bi_2O_3$ catalyst activation: effects of pH, inorganic anions, and water matrix, Chem. Eng. J. 338 (2018) 300–310, https://doi.org/10.1016/j.cej.2018.01.016.

[40] Y. Zheng, J. Yang, B.R.X.H. Zhang, J.F. Li, H.L. Zheng, G.P. Chen, C. Zhao, Hydraulic-driven piezo-activation of peroxymonosulfate for carbamazepine degradation with ultralow energy consumption, Chem. Eng. J. 441 (2022), 136116, https://doi.org/10.1016/j.cej.2022.136116.

[41] E.N. Ma, G.L. Sun, F.L. Duan, H.G. Wang, H. Wang, Visible-light-responsive Z-scheme heterojunction $MoS_2$ NTs/$CuInS_2$ QDs photoanode for enhanced photoelectrocatalytic degradation of tetracycline, Appl. Mater. Today 28 (2022), 101504, https://doi.org/10.1016/j.apmt.2022.101504.

[42] Y.X. Zhu, Y.J. Cui, B.B. Xiao, J. Ou-yang, H.P. Li, Z.R. Chen, Z-scheme 2D/2D g-$C_3N_4$/$Sn_3O_4$ heterojunction for enhanced visible-light photocatalytic $H_2$ evolution and degradation of ciprofloxacin, Mater. Sci. Semicond. Process 129 (2021), 105767, https://doi.org/10.1016/j.mssp.2021.105767.

[43] T.T. Cheng, W.H. Gao, H.J. Gao, S.F. Wang, Z. Yi, X.X. Wang, H. Yang, Piezocatalytic degradation of methylene blue, tetrabromobisphenol A and tetracycline hydrochloride using $Bi_4Ti_3O_{12}$ with different morphologies, Mater. Res. Bull. 141 (2021), 111350, https://doi.org/10.1016/j.materresbull.2021.111350.

[44] S. Zhang, H.X. Liu, F.X. Gao, M. Fang, Y.F. Zhang, Y.W. Cai, M.G. Kong, X.L. Tan, The synergetic enhancement of piezo catalytic performance to remove tetracycline by $K_2Ti_6O_{13}$/$TiO_2$ composite, J. Alloy. Compd. 900 (2022), 163492, https://doi.org/10.1016/j.jallcom.2021.163492.

[45] P.S. Selvamani, J.J. Vijaya, L.J. Kennedy, A. Mustafa, M. Bououdina, P.J. Sophia, R. J. Ramalingam, Synergic effect of $Cu_2O$/$MoS_2$/rGO for the sonophotocatalytic degradation of tetracycline and ciprofloxacin antibiotics, Ceram. Int. 47 (2021) 4226–4237, https://doi.org/10.1016/j.ceramint.2020.09.301.

[46] C. Zhou, W.C. Liu, H.Q. Li, M. Yang, Z.X. Yang, Separable magnetic $Fe_3O_4$@$MoS_2$ composite for adsorption and piezo-catalytic degradation of dye, Catalysts 11 (2021) 1403, https://doi.org/10.3390/catal11111403.

[47] Z.Y. Li, Q.L. Zhang, L.K. Wang, J.Y. Yang, Y. Wu, Y.M. He, Novel application of Ag/$PbBiO_2I$ nanocomposite in piezocatalytic degradation of rhodamine B via harvesting ultrasonic vibration energy, Ultrason Sonochem. 78 (2021), 105729, https://doi.org/10.1016/j.ultsonch.2021.105729.

[48] B.J. Huo, F.Q. Meng, J.W. Yang, Y.L. Wang, J.G. Qi, W. Ma, Z.C. Wang, J.X. Wang, Z.H. Wang, High efficiently piezocatalysis degradation of tetracycline by few-layered $MoS_2$/GDY: mechanism and toxicity evaluation, Chem. Eng. J. 436 (2022), 135173, https://doi.org/10.1016/j.cej.2022.135173.

[49] Z.W. Liu, K. Zhao, G.X. Xing, W.X. Zheng, Y.F. Tang, One-step synthesis of unique thorn-like $BaTiO_3$–$TiO_2$ composite nanofibers to enhance piezo-photocatalysis performance, Ceram. Int. 47 (2021) 7278–7284, https://doi.org/10.1016/j.ceramint.2020.11.017.

[50] X.G. Li, Y.X. Guo, L.G. Yan, T. Yan, W. Song, R. Feng, Y.W. Zhao, Enhanced activation of peroxymonosulfate by ball-milled $MoS_2$ for degradation of tetracycline: Boosting molybdenum activity by sulfur vacancies, Chem. Eng. J. 429 (2022), 132234, https://doi.org/10.1016/j.cej.2021.132234.

[51] B. Sheng, F. Yang, Y.H. Wang, Z.H. Wang, Q. Li, Y.G. Guo, X.Y. Lou, J.S. Liu, Pivotal roles of $MoS_2$ in boosting catalytic degradation of aqueous organic pollutants by Fe (II)/PMS, Chem. Eng. J. 375 (2019), 121989, https://doi.org/10.1016/j.cej.2019.121989.

[52] R. Bai, W.F. Yan, Y. Xiao, S.Q. Wang, X.C. Tian, J.P. Li, X.F. Xiao, X.Q. Lu, F. Zhao, Acceleration of peroxymonosulfate decomposition by a magnetic $MoS_2$/$CuFe_2O_4$ heterogeneous catalyst for rapid degradation of fluoxetine, Chem. Eng. J. 397 (2020), 125501, https://doi.org/10.1016/j.cej.2020.125501.

[53] S.Y. Lan, C. Yu, E.Y. Wu, M.S. Zhu, D.D. Dionysiou, Self-powered water flow-triggered piezocatalytic generation of reactive oxygen species for water purification in simulated water drainage, ACS EST Eng. 2 (2022) 101–109, https://doi.org/10.1021/acsestengg.1c00296.

[54] X.M. Liao, H.Y. Xie, B.R. Liao, S. Hou, Y. Yu, X.Y. Fan, Ball milling induced strong polarization electric fields in Cu3B2O6 crystals for high efficiency piezocatalysis, Nano Energy 94 (2022), 106890, https://doi.org/10.1016/j.nanoen.2021.106890.

[55] H. Lei, Q.S. He, M.X. Wu, Y.Y. Xu, P.F. Sun, X.P. Dong, Piezoelectric polarization promoted spatial separation of photoexcited electrons and holes in two-dimensional g-$C_3N_4$ nanosheets for efficient elimination of chlorophenols, J. Hazard. Mater. 421 (2022), 126696, https://doi.org/10.1016/j.jhazmat.2021.126696.

[56] M. Li, Y.W. Li, P.F. Yu, H.M. Zhao, L. Xiang, N.X. Feng, Q.K. Li, K.Y. He, X. Luo, Q. Y. Cai, S.Q. Zhou, C.H. Mo, K.L. Yeung, Exploring degradation mechanism of tetracycline via high-effective peroxymonosulfate catalysts of montmorillonite hybridized CoFe composites and safety assessment, Chem. Eng. J. 427 (2022), 130930, https://doi.org/10.1016/j.cej.2021.130930.

[57] Synthesis of $Fe_3O_4$/Pr-BiOCl/Luffa composites with enhanced visible light photoactivity for organic dyes degradation, Mater. Res. Bull. 106 (2018) 409–417, https://doi.org/10.1016/j.materresbull.2018.06.029.

[58] T. Jiang, T. Xie, L. Chen, Z. Fu, D. Wang, Carrier concentration-dependent electron transfer in $Cu_2O$/ZnO nanorod arrays and their photocatalytic performance, Nanoscale 5 (2013) 2938–2944, https://doi.org/10.1039/C3NR34219K.

[59] J.T. Zhao, P. Zhang, J.J. Fan, J.H. Hu, G.S. Shao, Constructing 2D layered $MoS_2$ nanosheets-modified Z-scheme $TiO_2$/$WO_3$ nanofibers ternary nanojunction with enhanced photocatalytic activity, Appl. Surf. Sci. 430 (2018) 466–474, https://doi.org/10.1016/j.apsusc.2017.06.308.

[60] Y.L. Liu, J.M. Wu, Synergistically catalytic activities of $BiFeO_3$/$TiO_2$ core-shell nanocomposites for degradation of organic dye molecule through piezophototronic effect, Nano Energy 56 (2019) 74–81, https://doi.org/10.1016/j.nanoen.2018.11.028.

[61] L. Zhou, H. Li, X.X. Zhang, Y. Zhao, J. Wang, L.C. Pan, G.S. Du, Q. He, X.L. Li, Rapamycin treated tol-dendritic cells derived from BM- MSCs reversed graft rejection in a rat liver transplantation model by inducing $CD8^+CD45RC^-$Treg, Mol. Immunol. 137 (2021) 11–19, https://doi.org/10.1016/j.molimm.2021.03.018.

[62] Q.C. Zhang, L. Jiang, J. Wang, Y.F. Zhu, Y.J. Pu, W.D. Dai, Photocatalytic degradation of tetracycline antibiotics using three-dimensional network structure perylene diimide supramolecular organic photocatalyst under visible-light irradiation, Appl. Catal. B 277 (2020), 119122, https://doi.org/10.1016/j.apcatb.2020.119122.

[63] H.Y. Zhou, L.D. Lai, Y.J. Wan, Y.L. He, G. Yao, B. Lai, Molybdenum disulfide ($MoS_2$): a versatile activator of both peroxymonosulfate and persulfate for the degradation of carbamazepine, Chem. Eng. J. 384 (2020), 123264, https://doi.org/10.1016/j.cej.2019.123264.
[64] X.G. Li, Y.X. Guo, L.G. Yan, T. Yan, W. Song, R. Feng, Y.W. Zhao, Enhanced activation of peroxymonosulfate by ball-milled $MoS_2$ for degradation of tetracycline: Boosting molybdenum activity by sulfur vacancies, Chem. Eng. J. 429 (2022), 132234, https://doi.org/10.1016/j.cej.2021.132234.
[65] B. Sheng, F. Yang, Y.H. Wang, Z.H. Wang, Q. Li, Y.G. Guo, X.Y. Lou, J.S. Liu, Pivotal roles of $MoS_2$ in boosting catalytic degradation of aqueous organic pollutants by Fe(II)/PMS, Chem. Eng. J. 375 (2019), 121989, https://doi.org/10.1016/j.cej.2019.121989.
[66] W. Liu, Y.Y. Li, F.Y. Liu, W. Jiang, D.D. Zhang, J.L. Liang, Visible-light-driven photocatalytic degradation of diclofenac by carbon quantum dots modified porous g-$C_3N_4$: Mechanisms, degradation pathway, and DFT calculation, Water Res. 151 (2019) 8–19, https://doi.org/10.1016/j.watres.2018.11.084.
[67] X.D. Zhang, F.K. Bi, Z.Q. Zhu, Y. Yang, S.H. Zhao, J.F. Chen, X.T. Lv, Y.X. Wang, J. C. Xu, N. Liu, The promoting effect of $H_2O$ on rod-like MnCeOx derived from MOFs for toluene oxidation: a combined experimental and theoretical investigation, Appl. Catal. B 297 (2021), 120393, https://doi.org/10.1016/j.apcatb.2021.120393.
[68] Y.C. Zhu, F. Wang, B.H. Zhou, H.L. Chen, R.F. Yuan, Y.Y. Zhang, H.H. Geng, Y. X. Liu, H. Wang, Photo-assisted $Fe^{2+}$ modified molybdenum disulfide activated potassium persulfate to degrade sulfadiazine: Insights into the degradation pathway and mechanism from density functional theory, Chem. Eng. J. 435 (2022), 134904, https://doi.org/10.1016/j.cej.2022.134904.
[69] Y. Kato, H. Matsumoto, T. Mori, Absence of HOMO/LUMO transition in charge-transfer complexes of thienoacenes, J. Phys. Chem. A 125 (2021) 146–153, https://doi.org/10.1021/acs.jpca.0c08925.
[70] Y. Yang, J.L. Zhang, L.H. Shen, L.J. Feng, Q. Zhou, Inhibition mechanism of diacylated anthocyanins from purple sweet potato (Ipomoea batatas L.) against α-amylase and α-glucosidase, Food Chem. 359 (2021), 129934, https://doi.org/10.1016/j.foodchem.2021.129934.
[71] N. Tian, X.K. Tian, Y.L. Nie, C. Yang, Z.X. Zhou, Y. Li, Biogenic manganese oxide: an efficient peroxymonosulfate activation catalyst for tetracycline and phenol degradation in water, Chem. Eng. J. 352 (2018) 69–76, https://doi.org/10.1016/j.cej.2018.07.061.
[72] Y. Zhang, J.B. Zhou, X. Chen, L. Wang, W.Q. Cai, Coupling of heterogeneous advanced oxidation processes and photocatalysis in efficient degradation of tetracycline hydrochloride by Fe-based MOFs: synergistic effect and degradation pathway, Chem. Eng. J. 369 (2019) 745–757, https://doi.org/10.1016/j.cej.2019.03.108.
[73] J. Hoigné, H. Bader, Kinetics of reactions of chlorine dioxide (OClO) in water—I. Rate constants for inorganic and organic compounds, Water Res 28 (1994) 45–55, https://doi.org/10.1016/0043-1354(94)90118-X.